LASER INTERFEROMETER GRAVITATIONAL WAVE OBSERVATORY

LIGO Laboratory / LIGO Scientific Collaboration

LIGO-T020027-00-D *ADVANCED LIGO* 04/03/02

Input Optics Subsystem Conceptual Design Document

R. Amin, G. Mueller, M. Rahkmanov, D. Reitze, D.B. Tanner, S. Wise

Distribution of this document:
LIGO Science Collaboration

This is an internal working note
of the LIGO Project.

California Institute of Technology
LIGO Project – MS 18-34
1200 E. California Blvd.
Pasadena, CA 91125
Phone (626) 395-2129
Fax (626) 304-9834
E-mail: info@ligo.caltech.edu

Massachusetts Institute of Technology
LIGO Project – NW17-161
175 Albany St
Cambridge, MA 02139
Phone (617) 253-4824
Fax (617) 253-7014
E-mail: info@ligo.mit.edu

LIGO Hanford Observatory
P.O. Box 1970
Mail Stop S9-02
Richland WA 99352
Phone 509-372-8106
Fax 509-372-8137

LIGO Livingston Observatory
P.O. Box 940
Livingston, LA 70754
Phone 225-686-3100
Fax 225-686-7189

http://www.ligo.caltech.edu/

Table of Contents

Table of Tables

Table of Figures

Abstract

This document outlines the conceptual design for the Advanced LIGO Input Optics Subsystem. The IO design is consistent with the requirements listed in LIGO-T020020-00-D, "Input Optics Subsystem Design Requirements Document." The Input Optics Subsystem includes the RF modulation of the light, the input mode cleaner, mode matching of the light to the interferometer, and beam steering into the interferometer. The scope of the IO includes the following hardware: phase modulation Pockels cells, photodetectors and related protective shutter, active jitter suppression system, mode cleaner optics, suspensions, Faraday isolator, and mode matching telescopes.

1 Introduction

1.1 Input Optics Conceptual Design: Overview

1.1.1 Interferometer System Context

The Input Optics act as a bridge between the prestabilized laser light of the PSL subsystem and the LIGO interferometer core optics. It also provides signals to the Interferometer Sensing and Control subsystems. The IO performs frequency and pointing stabilization, and mode matches the light to the mode defined by the Core Optics. The IO also provides for phase modulation of the light and signal extraction of the IFO reflected light.

1.1.2 System Components

The Input Optics (IO) subsystem consists of the following units, schematically shown in figure 1:

- RF Modulators
- Out of Vacuum Steering and Conditioning Optics (MC MMT, jitter suppression, MC input steering)
- Mode Cleaner
- PSL Intensity Stabilization Signal
- Faraday Isolation/IFO Signal Extraction
- IFO Mode Matching and Beam Pointing

Figure 1 IO Conceptual Layout

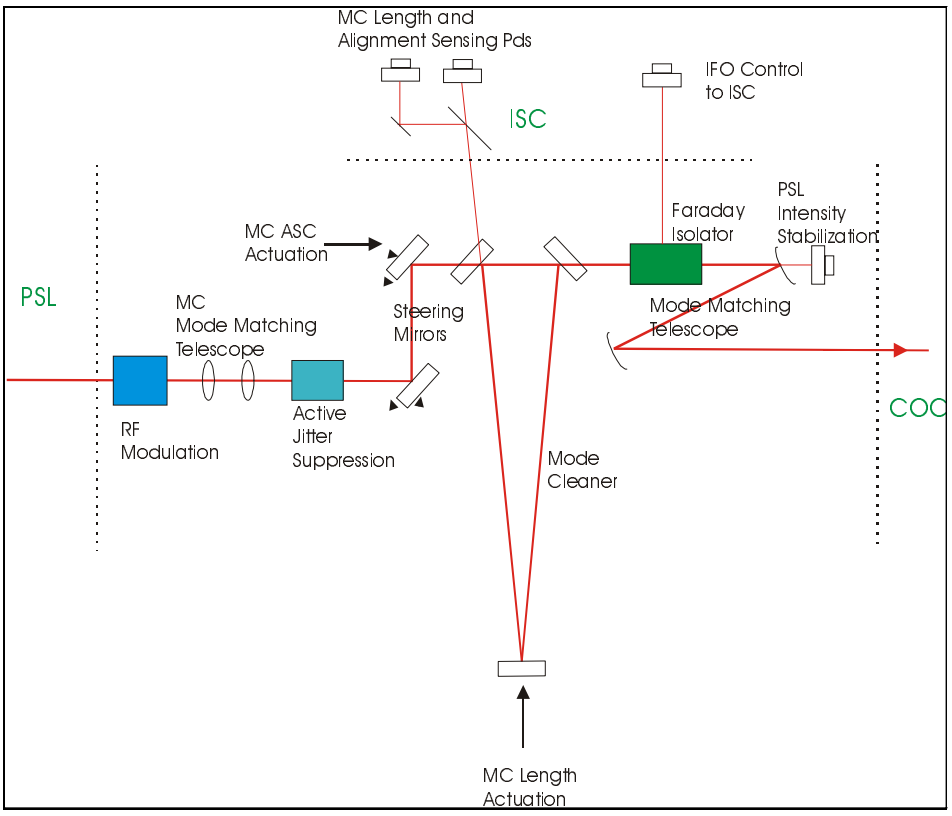

1.1.3 Design Philosophy

Guided by IO functional requirements and design simplicity, we envision the Advanced IO to be conceptually quite similar to the LIGO I Input Optics. In addition, lessons learned from LIGO I have been incorporated into the design.

1.2 Definitions

- Low Frequency = $f < 10$ Hz
- In-band = 10 Hz – 10 kHz

1.3 Acronyms

ASC - Alignment Sensing and Control
BS – Beamsplitter
BSC – BeamSplitter Chamber, a vacuum chamber
CDS - Control and Data Systems
COC - Core Optics Components
DRD - Design Requirements Document
ETM – End Test Mass
FOM – Figure of Merit
FSR – Free Spectral Range
GW - Gravitational Wave
HAM – Horizontal Access Module, a vacuum chamber
IFO - LIGO interferometer
IO – LIGO Input Optics
ISC - Interferometer Sensing and Control
ITM – Input Test Mass
LHO – LIGO Hanford Observatory
LLO – LIGO Livingston Observatory
LSC – Length Sensing and Control
MC - Mode Cleaner
MMT – Mode Matching Telescope
PRM – Power Recycling Mirror
PSL - Prestabilized laser
RF - Radio Frequency
RFAM – Radio Frequency Amplitude Modulation
RIN – Relative Intensity Noise
SEI - Seismic Isolation
SRM – Signal Recycling Mirror
SRS - Software Requirement Specification
SUS - Suspension Control
SYS - Detector Systems Engineering
TBA – To Be Added
TBD - To Be Determined
TBR – To Be Revised

TLA – Three Letter Acronym

1.4 Applicable Documents

1.4.1 LIGO Documents

[1] LIGO-T010075, "Advanced LIGO Systems Design," P. Fritschel, et al.

[2] LIGO-M990288, "LIGO 2 Conceptual Project Book"

[3] LIGO-E990303, "Seismic Isolation Subsystem Design Requirements Document," P. Fritschel, et al.

[4] LIGO-T010076, "Optical Layout for Advanced LIGO," D. Coyne

[5] LIGO-T020022, "Pointing Requirements in Advanced LIGO, Part I," G. Mueller, et al.

[6] LIGO T020021, "Sideband Requirements in Advanced LIGO, Part I," G. Mueller, et al.

[7] LIGO T020025, "EO-Modulators for Advanced LIGO, Part I," G. Mueller et al.

[8] LIGO-T000053-01-D "Cavity Optics Suspension Subsystem Design Requirements Document, P. Willems, et al.

1.4.2 Non-LIGO Documents

[1] E. Khazanov, N. Andreev, A. Babin, A. Kiselev, O. Palashov, and D. H. Reitze, "Suppression of Self-Induced Depolarization of High-Power Laser Radiation in Glass-Based Faraday Isolators, J. Opt. Soc. Am B. **17**, 99-102 (2000).

[2] Justin D. Mansell, Joseph Hennawi, Eric Gustafson, Martin Fejer, Robert L. Byer, David Clubley, S. Yoshida, and D. H. Reitze, "Evaluating the effect of transmissive optic thermal lensing on laser beam quality using a Shack-Hartmann wavefront sensor", Appl. Opt. **40**, 366-374 (2001).

[3] Efim A. Khazanov, Nikolay N. Andreev, Oleg V. Palashov, Oliver Mehl, and D. H. Reitze, "Effect of TGG crystal orientation on the isolation ratio of the Faraday isolator at a high average power", Appl. Opt. **41**, 483-492 (2002).

[4] "Method for Compensation of Thermally-induced Modal Distortions in the Input Optical Components of Gravitational Wave Interferometers," G. Mueller et al., accepted for publication in a special issue of *Classical and Quantum Gravity*, to appear, 05/2002.

2 General Design

2.1 IO System Layout

A schematic diagram of the positions of the input optics components both outside and within the vacuum chamber is shown in Figure 2. Optics not in vacuum are mounted on the same table as the PSL in a clean, enclosed, and acoustically/seismically stable environment. All optics in vacuum will be mounted on vibration isolation stacks. With the exception of the Faraday isolator and MC input steering mirrors, all main IFO beam optics including and following the mode cleaner will be suspended. Diagnostic beam optics for IFO and MC control will be located on fixed mounts. Output ports in the HAMs will be used as optical feedthroughs for sensing beams.

2.2 Possible Methods for Minimizing Frequency Noise Due to Acoustic Coupling to Mirror Mounts and Periscopes

LIGO 1 has suffered from coupling of acoustic noise in the PSL/IOO table environment to mirror mounts. In addition, the table surface was not stiff enough to constrain the (heavy) periscope frame first employed; eventually a lighter design was used. Possible treatments for the acoustic noise problem are:

1) enclose PSL components in separate vacuum (with suitable vibration isolation).

2) provide low-acoustic (anechoic) enclosure around PSL with all noise producing (fans, etc) devices outside this enclosure.

Possible treatments to the periscope problem are:

1) move periscope into vacuum system (requires a HAM viewport at table level).

2) raise table to eliminate periscope.

Both treatments are outside the scope of the IOO subsystem alone.

Figure 2 - Conceptual Layout of IO Components on the PSL Table and on HAMS

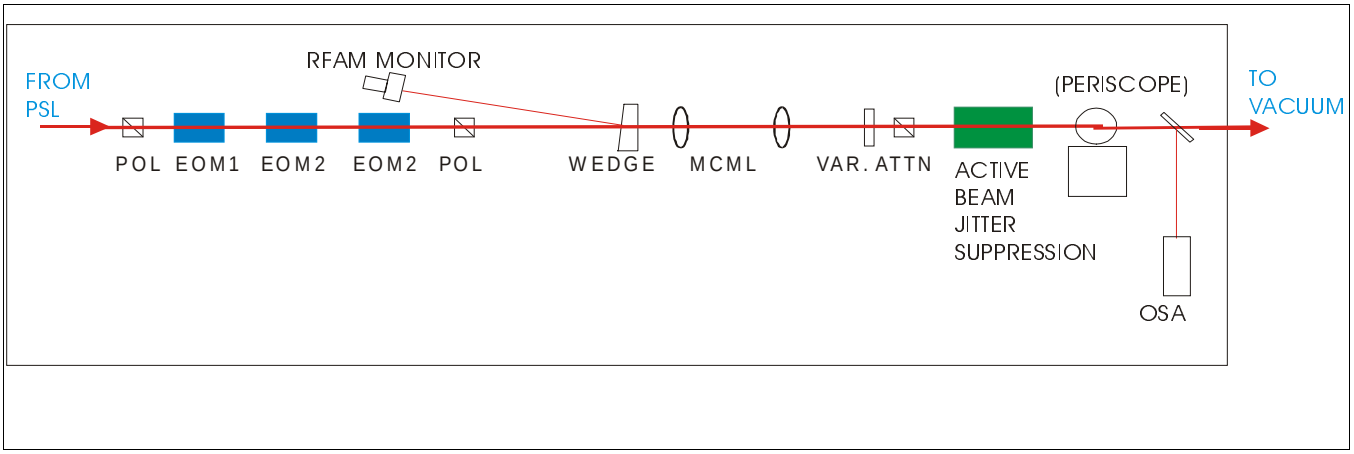

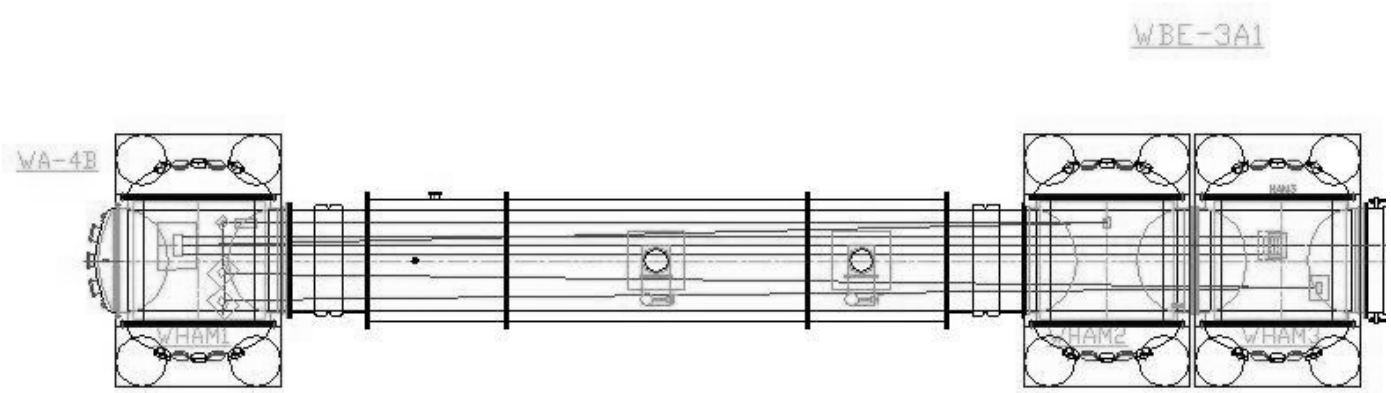
WBE-3A1
WA-4B
WHAM1
WHAM2
WHAM3

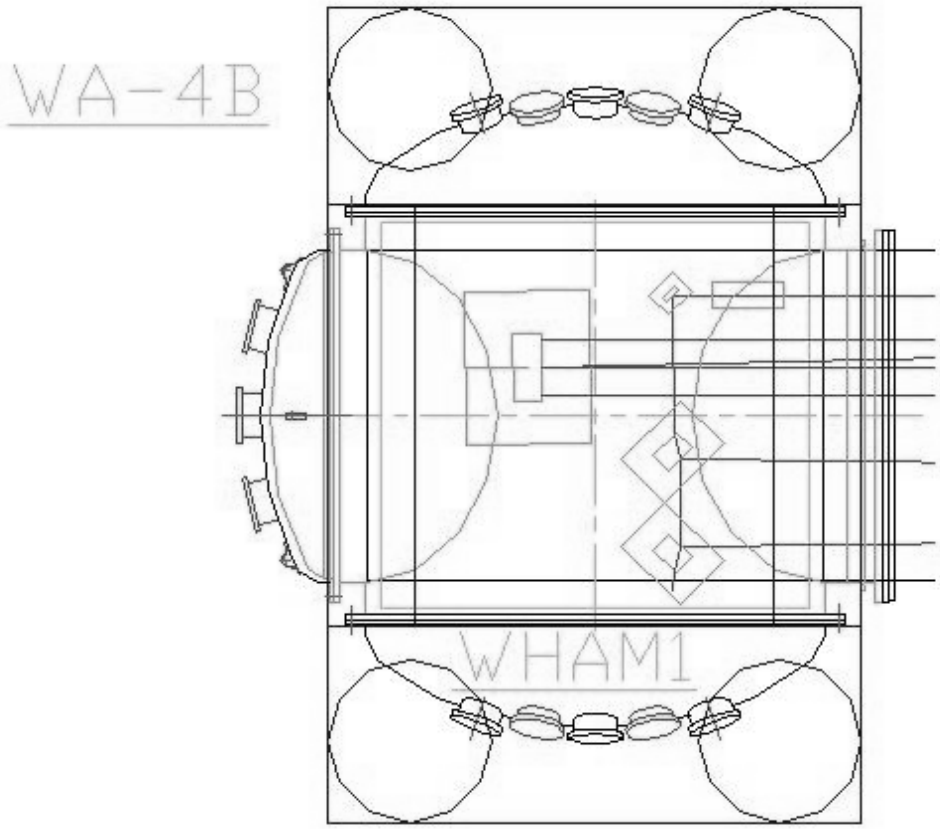
WA-4B
WHAM1

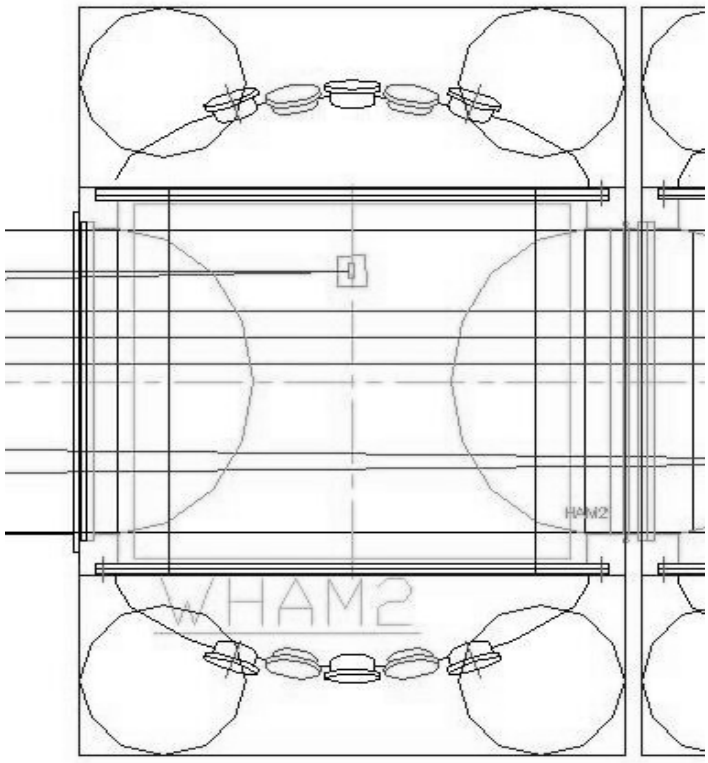
HAM2
WHAM2

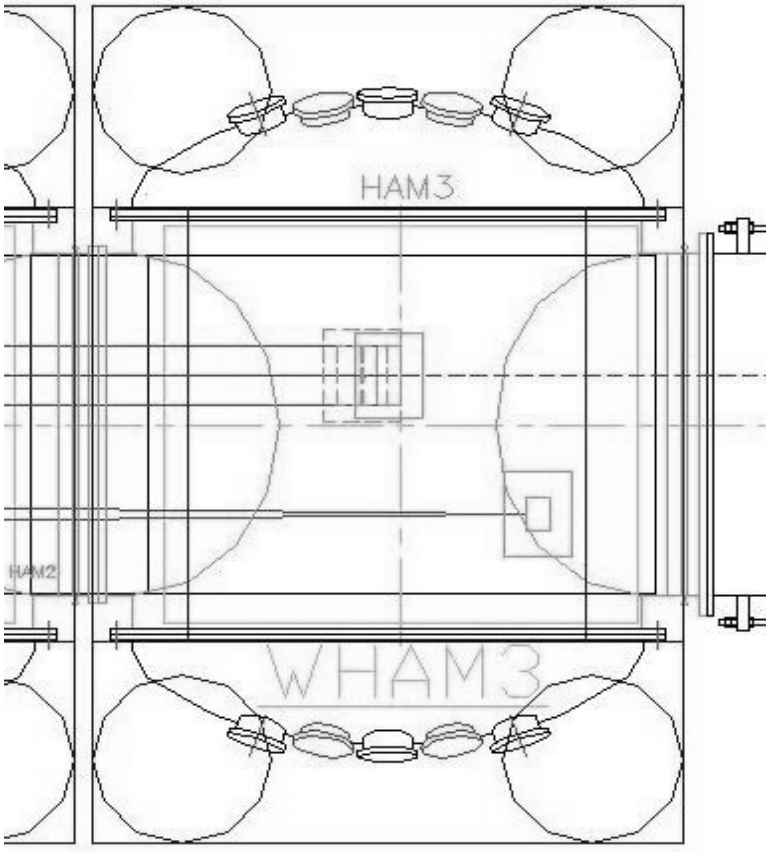
HAM3
HAM2
WHAM3

2.2.1 Dimensional Constraints

Relevant dimensions are given in the following table. Components of the IO system are located on the PSL table and HAMs 1, 2, and 3. HAM3 also holds the recycling mirror.

Table 1 Relevant Dimensions

Item	*Unit*	*Value*
HAM1(7) - HAM2(8) spacing (center-center)	m	13.72
HAM2(8) - HAM3(9) spacing (center-center)	m	2.63
HAM1(7) stack area dimensions (L x W)	m x m	1.90 *x* 1.70 (TBR)
HAM2(8) stack area dimensions (L x W)	m x m	1.90 *x* 1.70 (TBR)
HAM3(9) stack area dimensions (L x W)	m x m	1.90 *x* 1.70 (TBR)
HAM1,2 (7,8) Connecting Beam Tube Diameter	m	1.2*
Δz (HAM1-HAM2, local coordinates, LHO)	mm	8.49†
Δz (HAM2-HAM3, local coordinates, LHO)	mm	1.59†
Δz (HAM7-HAM8, local coordinates, LHO)	mm	-8.49†
Δz (HAM8-HAM9, local coordinates, LHO)	mm	-1.59†
Δz (HAM1-HAM2, local coordinates, LLO)	mm	4.28†
Δz (HAM2-HAM3, local coordinates, LLO)	mm	0.80†
PSL table area dimensions	ft x ft	16 x 5

* Given requirements on the sizes of the MC mirrors and suspensions, the current HAM1,2 and HAM 7,8 beam tube must be replaced with standard LIGO I beam tubes to be able to accommodate the in-vacuum IO components.

† As viewed from the vertex, the LHO X axis slopes downward by 0.619 mrad and the Y axis slopes upward by 0.012 mrad. WHAM1 is 8.5 mm higher (compared with local level) than WHAM2. WHAM7 is 8.5 mm lower (compared with local level) than WHAM8. At LLO things are different of course: the LHO X axis slopes downward by 0.312 mrad and the Y axis slopes downward by 0.612 mrad. LHAM1 is 4.3 mm higher than LHAM2.

2.3 Overall IO Efficiency

The IO must deliver 76% of the TEM_{00} light emerging from the PSL to the IFO, including all integrated losses from reflection, transmission, and absorption in the IO optical components, as well as light lost into uncompensated higher order modes through thermal lensing. The following table shows the transmission of the components of the IO components. For the suspended components, we have assumed coatings similar those achieved in the LIGO I IO, i.e., roughly 50 ppm loss.[1] Small optics are assumed to have antireflection coatings that match the standard

[1] LIGO Director's Review, 2/14/00?? G00xxxx?

commercial narrowband multilayer coatings (0.1%). Out-of-vacuum optics are assumed to have higher scatter loss (200 ppm). Losses of TEM_{00} mode in the RF modulators and Faraday isolator are based on conservative estimates of passive thermal lensing compensation using $-dn/dT$ values for FK51 Schott glass.

Table 2 Estimated IO Efficiency

Item	*Absorbance and Reflectance Loss*	*TEM_{00} Mode Loss*	*TEM_{00} Transmittance*	*Integrated Transmittance*
RF modulators and lenses	0.035	0.04[2]	0.925	**0.925**
PSL mirrors (2)	0.002	0	0.998	**0.923**
MC mode matching lenses (3)	0.002	0.0001	0.9979	**0.921**
HAM1 viewport window	0.006	0.001	0.993	**0.915**
MC injection mirrors (3)	0.0006	0	0.9994	**0.914**
Mode cleaner	0.05[3]	0.001	0.949	**0.868**
Faraday isolator	0.05	0.025[4]	0.925	**0.805**
Steering mirror	0.033[5]	0	0.967	**0.778**
Telescope negative mirror	0.0002	0	0.9998	**0.778**
Telescope converging mirror	0.0002	0	0.9998	**0.778**
Mode Matching Efficiency	0	0.015	0.985	**0.763**

[2] Based on preliminary measurements of thermal lensing in rubidium titanyl arsenate.

[3] Losses include mode mismatch and cavity visibility; estimate based on conservative LIGO 1 result.

[4] "Method for Compensation of Thermally-induced Modal Distortions in the Input Optical Components of Gravitational Wave Interferometers," G. Mueller et al., accepted for publication in a special issue of *Classical and Quantum Gravity*, to appear, 05/2002.

[5] Assumes 5W needed for PSL intensity stabilization; TBD.

3 RF Modulation

3.1 Introduction

The modulation of 165 W of CW laser power requires a substantial testing effort to determine which electro-optically active materials, if any, are suitable in terms of:

- long term power handling capabilities (damage)
- thermal beam distortions due to laser and RF heating
- sufficiently low second harmonic generation efficiency
- adequate modulation response (frequency and depth)
- suitable amplitude and phase stability

Based on our research and optical testing of modulator materials to date, we believe that serial modulation will suffice for Advanced LIGO.

3.2 Modulator Material Selection

3.2.1 Optical and Electro-optical Properties

After a literature survey and consultation with Crystal Associates and Raicol Corporation, we are focusing on 5 different materials: potassium titanyl phosphate (KTP), potassium titanyl arsenate (KTA), rubidium titanyl arsenate (RTA), rubidium titanyl phosphate (RTP), and lithium niobate ($LiNb0_3$). A summary of the known material and optical properties is shown in Table 3

Table 3 Material Parameters for Selected EOM Crystals

Properties	KTP	KTA	RTA[6]	RTP[7]	$LiNbO_3$
Laser Damage Threshold [MW/cm^2, 10ns,1064nm]	600 (AR coated)	400	400	600 (AR coated)	280[8]
n_x @ 1064nm	1.748	1.788	1.811	1.9[9]	2.23
n_y @ 1064nm	1.756	1.796	1.815	1.9[9]	2.23
n_z @ 1064nm	1.840	1.878	1.890	1.9[9]	2.16

[6] data from Crystal Associates

[7] data from Raicol

[8] Number from Raicol's web page

[9] Raicol gives only one index of refraction. Because of the crystal structure, the principal components have to be different; nevertheless, on account of the similarity between RTA and RTP, the differences will be very modest.

Absorption coefficient[10] α @ 1064nm [1/cm]	< 0.5%	< 0.5%	< 0.5%	< 0.5%	< 0.5%
EO-Coef. (pm/V)@633nm					
r_{33}	36.3	37.5	40.5	39.6	30.8
r_{23}	15.7	15.4	17.5	17.1	8.6
r_{13}	9.5	11.5	13.5	12.5	8.6
r_{42}	9.3	?	?	?	28
r_{51}	7.3	?	?	?	28
r_{22}					3.4
$n_z^3\, r_{33}$	226	248	273	272	306
Electrical (640 kHz, 22°C)					
Dielectric ε_{33}	23	44	19	13	
Conductivity σ_{33} (1/Ωcm)	6×10^{-6}	5×10^{-5}	3×10^{-9}	$\sim10^{-11}$	
Loss Tangent d_{33}	0.7	2.9	.0004	?	

The largest EO-coefficient is in all five materials r_{33}. The optimum configuration is propagation direction in the y-direction; applied electrical field and polarization of the light field in the z-direction. The modulation depth is given by:

$$\Delta\Phi = m = \frac{\pi L}{\lambda} r_{33} n_z^3 \frac{U_z}{d}$$

where L is the length of the crystal, U_z the voltage across the crystal, and d the thickness in the z-direction. $LiNbO_3$ requires the lowest drive voltage, but, as we will see later, is not useful because of thermal problems.

[10] The absorption coefficient given here is only a very rough upper limit. In fact, the measured thermal lensing in RTA indicates a considerably smaller absorption coefficient. Raicol claim that their KTP crystals have absorption below 50ppm/cm. RTP will be of the same order.

RTA and RTP require a 10% larger drive voltage. Based on these data we decided to study both materials with RTP being our first choice because of the lower electrical loss angle and higher laser damage threshold. The modulation depth of $m = 0.5$ requires for RTA and RTP:

$$U_z \frac{L}{d} = 620V$$

The disadvantages of RTA and RTP are:

- crystals are only recently available in reasonable sizes
- much thermal data are unknown

The actual design (see 3.2.4) requires two crystals for each modulator:

- Size of each crystal at least 4mm x 4mm x 15mm
- Probably rotated by 90 deg with a half-wave plate or a quartz rotator in between

For this design, a voltage of

$$U_Z = 620\ V \frac{d}{2L} = 83\ V$$

is required across the crystal. The low electric conductivity or huge resistivity of RTP reduces the electric power consumption inside the crystal to:

$$P = UI = \frac{U_Z^{\,2}}{R} = \frac{(83V)^2}{10^{11}\Omega}\frac{L}{d}W = 30\ nW$$

In RTA, we expect ~100 times larger heat generation. However, the electrical heat generation is certainly dominated by the background resistivity of the leads and the electrodes. Moreover, the heat produced by the laser beam itself is more critical because of its nonuniform spatial distribution.

3.2.2 Thermal Properties

KTP and $LiNb0_3$ are fairly well characterized materials. Unfortunately, the thermal properties of RTA, RTP, and KTA are to a great extent unknown. Because of the similarities between RTA, RTP, KTP, and KTA, we expect that the properties are similar to KTP. All thermal problems scale with the parameter Q:

$$Q \equiv \frac{dn}{dT}\frac{\alpha}{\kappa}$$

Table 4 Thermal Properties for Various EOM materials

Properties	KTP	$LiNb0_3$
dn_x/dT [10^{-6}/K]	11 [a]	5.4 [b]

dn_y/dT [10^{-6}/K]	13 [a]	5.4 [b]
dn_z/dT [10^{-6}/K]	16[a]	37.9 [b]
κ_x [W/mK]	2	5.6[c]
κ_y [W/mK]	3	5.6[c]
κ_z [W/mK]	3	5.6[c]

[a] Handbook of Optics, no wavelength specified, [b] Crystal Technology, Inc. [c] only one value given, no axis specified.

$LiNbO_3$: Note that there exists a large difference in the ratios of *dn/dT* in $LiNbO_3$, resulting in a large ellipticity in the beam profile as observed in some of our experiments. In addition, surface damage was also occasionally observed at > 30 W powers. Thus, we believe that $LiNbO_3$ will not suffice as a modulator material for Advanced LIGO.

KTP: Comparing KTP to $LiNbO_3$, the ratio between *dn/dT* and κ for the z-axis in $LiNbO_3$ and the worst case in KTP is similar. The expected thermal lens can be approximated from the sag change over the beam profile:[11]

$$\delta s \approx 0.1\frac{\alpha LP}{\kappa}\frac{dn}{dT} \approx 2.4\mu m\frac{\alpha}{[10^{-2}/cm]}\frac{L}{[1.5cm]}\frac{P}{[200W]}$$

For an absorption coefficient of α=5x10^{-3}/cm, the sag change is roughly in the order of one wavelength. This leads to a thermal lens of

$$f \approx \frac{w^2}{\delta s} \approx 1m\left(\frac{w}{[mm]}\right)^2\left(\frac{[\mu m]}{\delta s}\right)$$

The amount of higher order modes that cannot be compensated by changes in the mode matching can then be found.[12] For a 0.5% absorption, we estimate that 20% of the light would be lost in each crystal. For the 6-crystal design envisioned above, essentially all of the light would shift into higher order modes. However, the absorption coefficients given in Table 3 include also non-thermal losses, including scattering, 2nd harmonic generation, etc. Therefore, the absorption values are upper limits for the thermal problems we could expect. It is possible that heat producing absorption coefficient will be much lower. According to information from different sources, the heat producing absorption coefficient in KTP is much lower than in $LiNbO_3$.

---

[11] Justin D. Mansell, Joseph Hennawi, Eric Gustafson, Martin Fejer, Robert L. Byer, David Clubley, S. Yoshida, and D. H. Reitze, "Evaluating the effect of transmissive optic thermal lensing on laser beam quality using a Shack-Hartmann wavefront sensor", Appl. Opt. **40**, 366-374 (2001).

[12] ibid

RTP and RTA: Raicol reports a total absorption coefficient for RTP as low as 50 ppm/cm (including scattering and 2nd harmonic generation), two orders of magnitude lower than the absorption coefficient used above. The subsequent sag change in the beam would be about 1% of the optical wavelength for 200 W power, the thermally induced lens in the 100 m range in each crystal, and a higher-order mode content less than a percent. Figure 3 displays the fraction of light remaining in a TEM_{00} mode as a function of laser power measured using a Fabry-Perot analyzer cavity. (For a discussion of the measurement technique, see Mueller, et al.[13])

Figure 3 Thermal Lensing in RTP

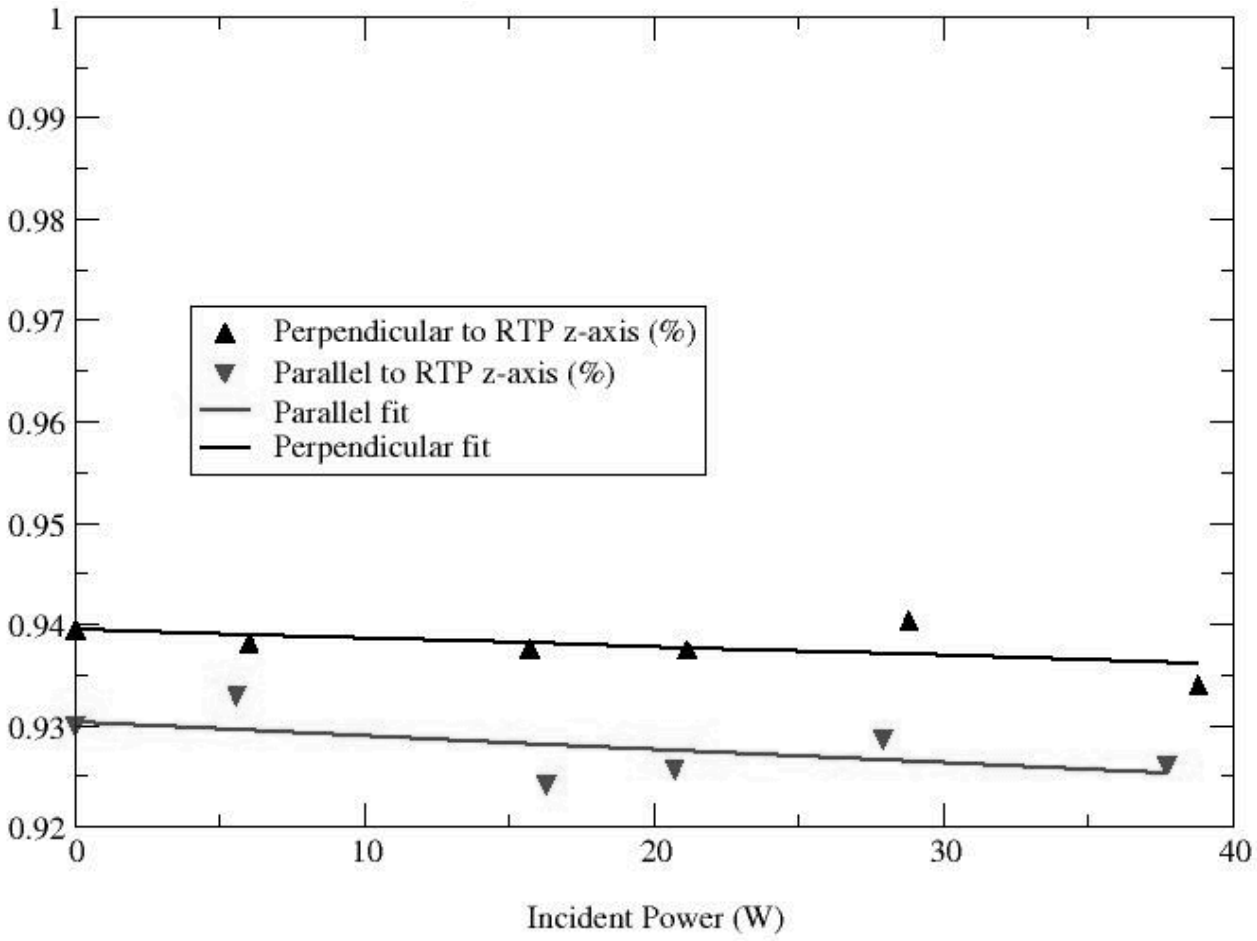

The data indicates that the light in the TEM_{00} remains relatively constant vs. incident power out to 40W. The residual higher order mode present at 0W is due to a combination of the mode content of the incident laser beam and the alignment in the analyzer cavity. RTP and RTA show the most promise as EOM materials for advanced LIGO.

[13] "Method for Compensation of Thermally-induced Modal Distortions in the Input Optical Components of Gravitational Wave Interferometers," G. Mueller et al., accepted for publication in a special issue of *Classical and Quantum Gravity*, to appear, 05/2002.

In the event that the thermal lensing in EOMs results in large (>4%) thermal lensing, a passive thermal compensation scheme can be implemented.[14]

3.2.3 Sideband Stability

In addition to the thermal issues and birefringence, the phase and amplitude stability of the sidebands is of some concern. The requirements depend strongly on the sensing scheme used and the bandwidth of the various feedback loops.[15]

The requirements in both sensing schemes depend on the modulation index. Although the modulation index is not yet set, it is very likely that the modulation index in a RF-Sensing scheme has to be larger than in a DC-Sensing scheme. This and the lower requirements at higher frequencies favor again the DC-Sensing scheme. But our goal has to be to reach the RF-Sensing scheme requirements.

The modulation index is given by:

$$m = \frac{\pi L}{\lambda} r_{33} n_z^3 \frac{U_z}{d}$$

3.2.3.1 Voltage

The capacitance of the electrodes at each crystal is about 1.7 pF. The current necessary to produce the required voltage (m=0.5) at a frequency f can be calculated from

$$I_c = 2\pi f C U_z$$

This is equivalent to 10^{18} electrons per sec and the shot noise is therefore

$$\Delta I_{SN} = 0.16 \frac{nA}{\sqrt{Hz}} \quad \Rightarrow \quad \Delta V_{SN} = 84 \frac{nV}{\sqrt{Hz}}$$

This is the shot noise without a resonance circuit.

3.2.3.2 Temperature

The temperature dependence of the following quantities must be considered:

- Index of refraction
- Electro optical coefficient r_{33}
- Dimensions

---

[14] "Method for Compensation of Thermally-induced Modal Distortions in the Input Optical Components of Gravitational Wave Interferometers," G. Mueller et al., accepted for publication in a special issue of *Classical and Quantum Gravity*, to appear, 05/2002.

[15] LIGO-T010075, "Advanced LIGO Systems Design," P. Fritschel, et al.

- Dielectric constant ε

Changes of the temperature will change the index of refraction. The modulation index will change with:

$$\delta m = \frac{\pi L}{\lambda}\frac{U_z}{d} r_{33} 3 n_z^2 \delta n \approx 1.5 \frac{[0.5]}{m}\frac{\delta n}{n}$$

Therefore the required stability of the index of refraction is:

$$\delta n < \frac{n}{3m^2}\frac{10^{-9}}{\sqrt{Hz}}\frac{f}{[10Hz]}$$

with

$$\delta n = \delta T \frac{dn}{dT}$$

The required temperature stabilization is thus:

$$\delta T < \left(\frac{dn}{dT}\right)^{-1} \frac{n}{3m^2}\frac{10^{-9}}{\sqrt{Hz}}\frac{f}{[10Hz]} \approx \frac{33\mu K}{\sqrt{Hz}}\frac{1}{m^2}\frac{f}{[10Hz]}$$

or about 0.13mK/sqrt(Hz) for a modulation index of 0.5.

The temperature dependence in the other parameters are not well known, but are expected to be in the same 10^{-5} range as the index of refraction; therefore, all lead to similar requirements for the temperature stability.

3.2.4 Modulator Design

Optical Layout

The final layout will depend on further experimental results and the availability of larger crystals. In the case that the thermally induced birefringence can be kept below the requirements in a single crystal modulator of sufficient length, each modulator will consist of only one single crystal. The direction of propagation is the x-axis; the applied electric field will be parallel to the polarization of the laser field and points in the z-direction. In the case that the thermally induced birefringence in a single crystal would not meet the requirements or that the available crystals would require a very large modulation voltage, it might be necessary to use two crystals for each modulator (Figure 4). Both crystals would be rotated by 90^o with respect to each other and between the crystals would be either a quartz rotator (QR) or a λ/2 plate to rotate the polarization by 90^o. This would in first order compensate the thermally induced birefringence and supply us with a reasonable modulation index at low drive voltages.

Figure 4 Modulator Design Concept

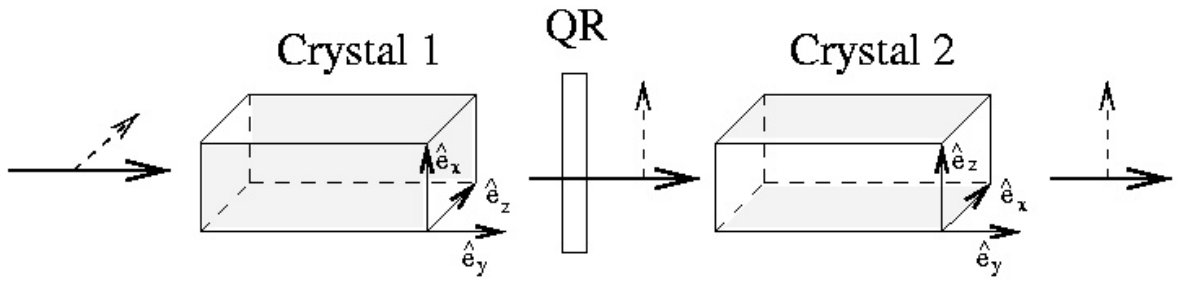

The crystals for further tests will have a surface of 4mm x 4mm. Clipping losses of a w=360µm Gaussian beam radius are below 60 ppm.

The intensity distribution in a Gaussian mode with total power P_o is:

$$P(r) = P_o \frac{2}{\pi} \frac{e^{-2\frac{r^2}{w^2}}}{w}$$

The intensity in the center is therefore:

$$P(r=0) \approx 100 \frac{kW}{cm^2}$$

approximately 6000 times below the damage threshold quoted for 10 ns pulses. Although still to be verified, it seems unlikely that this power level will damage the coatings (or crystals). Raicol quotes a damage threshold for the uncoated RTP crystals of 1 GW/cm^2.

Depending on the results of the experiments we will reevaluate the crystal dimensions and decide if a one-crystal design is sufficient or if we need to use two crystals.

B. Temperature Stabilization

It is planned to achieve the temperature stability with an active temperature control circuit. The temperature can be measured with standard low voltage temperature sensors like the TMP35/36/37 which has a sensitivity of 10mV/K. The temperature will be stabilized either by maintaining the crystal in an isothermal enclosure heated to about 30^o C or by feeding the error signal to Peltier elements that can cool the crystal from all four sides.

3.3 Modulator Test Plan

The following tests are planned to evaluate the suitability of RTP, RTA modulators in Advanced LIGO:

3.3.1 Optical Performance

Tests include:

- Determination of thermally-induced modal distortions under 180W loading and resonant RF drive voltage in a prototype two-crystal device. From these data, extrapolation to modal content after full modulator chain.
- Determination of thermally induced birefringence.
- Determination of continuous wave intensity damage threshold (I_{damage}).
- Operating at a safety margin of 0.1 I_{damage}, determination of the long term sustained (>500 hour) exposure performance.

3.3.2 Modulation Sideband Characteristics

- Measurement of the frequency dependent sideband amplitude stability (RFAM) at high laser powers
- Measurement frequency dependent frequency stability (to show limited by oscillator)

3.4 Contingency Modulation Schemes

Contingency modulations schemes (Mach-Zender modulation, frequency-locked subcarrier laser) will be investigated if the results of the high power testing warrant.

4 Active Jitter Suppression

For Advanced LIGO, the beam jitter required at the input of the MC is such that the relative amplitude of the TEM_{10} mode is:

$$a_{10}^{\max}(f) < 5\times10^{-7}\,\frac{1}{\sqrt{Hz}}$$

The pointing from the PSL is expected to be:

$$a_{10}^{PSL}(f) < 2\times10^{-6}\,\frac{1}{\sqrt{Hz}}$$

Given the maximum amount of filtering of the MC (limited by radiation pressure driven frequency noise), an external feedback loop is required to suppress this jitter to reach the MC input beam requirements. Although it is likely that the pointing coming from the laser decreases with higher frequencies, we simply don't know better and should be prepared to have a gain of about 4 up to a few kHz.

4.1 Detection of the pointing

4.1.1 RF Modulation/Demodulation via the ASC

The pointing could be measured with a modulation/demodulation scheme similar to the ones used for alignment sensing and control, albeit with higher bandwidth. The obvious RF frequency to use is the one that locks the mode cleaner length to the laser frequency. The primary purpose of this signal is to keep the mode cleaner aligned but it should also provide a signal to control the pointing of the laser beam. As neither the length sensing nor the alignment sensing systems are finalized yet, the details of this sensing scheme are not available yet. This scheme would measure at least in lowest order the position of the beam relative to the mode cleaner and would only in second order suffer from motion of the photodetector. (**Details TBD**)

4.1.2 Vacuum-based Quadrant Sensors

A second possibility would be to use segmented photodetectors, quad-detectors, or position detectors. A beam displacement equivalent to an amplitude of $5\text{x}10^{-7}$ in the TEM_{10} mode would shift the power in a segmented detector by about

$$\Delta P = P_1 - P_2 \approx 5\times10^{-7}\,\eta P_0$$

where P_1 and P_2 are the power levels in the two halves of the detector and η is the efficiency, which depends on the quantum efficiency of the photodetector material and also on the overlap integral between the TEM_{10} mode and the TEM_{00} mode in each half of the detector. The latter value depends, for example, on the thickness of the gap between the two halves. This efficiency will be in the order of 0.2 or better:

$$\Delta P \approx 10^{-7}\,P_0$$

This corresponds to a shot noise level of $P_o \approx 20\mu W$ *or* $I_{\min} \approx 20\mu A$

i.e., 1 mW for each photodetector should be sufficient.

The beam jitter shows up as both displacements and tilted phase fronts at the reference plane. It is therefore necessary to use two photodetectors at different planes. These measurement planes should be separated by a Gouy phase telescope that transforms a tilt in a phase front into a beam displacement. This requires either two photodetectors that measure vertical and horizontal displacement simultaneously (quad detectors), one at each reference plane, or two segmented photodetectors at each reference plane, one for the horizontal and one for the vertical direction, bringing the number of photodetectors up to four. As this scheme measures the position of the laser beam with respect to these photodetectors, it is mandatory to ensure that the positions of these photodetectors are stable with respect to the mode cleaner. **This requires that the photodetectors are installed on the HAM tables.** The details will depend on the available photodetectors and the footprints of them on the HAM tables.

4.2 Actuator requirements

The actuators should be able to correct the direction of the beam to suppress the TEM_{10} mode caused by the pointing. A TEM_{10} mode with an amplitude of a_{10}=2x10^{-6} would require a change in the direction of the beam of

$$2\times10^{-6} = \delta\beta\frac{\pi w}{\lambda} \quad \Rightarrow \quad \delta\beta \approx 7\times10^{-10}\,rad$$

for a w = 1 mm beam. As we assume a white noise spectrum, we need to provide this angular change over the full GW-band.

4.2.1 PZT Actuators

The standard way to change the beam pointing is to mount a mirror on two piezoelectric transducers (PZT). If we assume that the two PZTs are separated by 1cm, the necessary length change is given by

$$\Delta l \approx 7\,pm$$

The dynamic range of most appropriate PZTs exceeds this by far. The only problem seems to be the PZT resonances. The frequencies of these resonances depend on the PZT itself and the mass of the mirror. The use of light weight mirrors will increase the resonance frequency. Details: **TBD**.

4.2.2 RTP-prisms

Another possibility is the use of transparent crystals with high electro optic coefficients and low absorption coefficients. The obvious material in our case would be the material that we use for the electro-optical modulators: RTP. The design would require four small prisms, two for each direction, and two for each quadrature component of the tilt. For the ease of this analysis we assume that the beam enters each prism at normal incidence and leaves it under the angle β measured with respect to the second surface:

Figure 5 RTP-based Prism Actuator

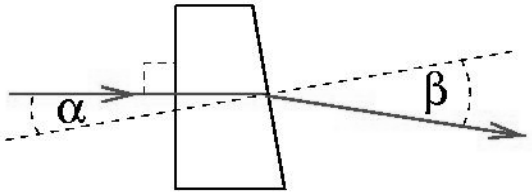

The beam deflection in a prism is

$$\sin\beta = n\sin\alpha$$

For small changes in the index of refraction this translates into:

$$\delta\beta = \frac{\delta n}{n}\tan\beta$$

The index of refraction of RTP is n=1.9. If we assume a α=10^o the static deflection angle will be β=19^o and we need to change the index of refraction by

$$\delta n = 4\times 10^{-9}$$

The change in the index of refraction in such electro-optical crystals is:

$$\delta n = \frac{1}{2}n^3 r_{33} E$$

where r_{33} is the electro-optic coefficient. For RTP we have $r_{33}n^3$ = 273 pm/V. The necessary electric field across the crystal is therefore:

$$E \approx 27\frac{V}{m} \qquad \Rightarrow \qquad U \approx 270mV\,\frac{d}{[10mm]}$$

or a voltage of around 270 mV across a 10 mm thick RTP crystal. The bandwidth would be easily available, because no piezo resonances will be present in the interesting frequency region. (**Details TBD**)

5 Mode Cleaner

5.1 Introduction

The suspended mode cleaner of the IO subsystem serves the following functions in stabilizing the laser light.

- In-band active frequency stabilization.
- Rejection of laser output that is not in the TEM_{00} mode. (Beam Jitter suppression.)
- Passive intensity and frequency stabilization above the cavity pole frequency.

5.2 Physical Characteristics

5.2.1 Parameters

Table 5 presents the physical characteristics of the mode cleaner consistent with the IO Design Requirements and Advanced LIGO optical layout,[16] the physical constraints imposed by the vacuum envelope.[17,18] These parameters are listed for a cold cavity (0 W) and a hot cavity (165 W).

Table 5 Mode Cleaner Physical Parameters

Definition	*Unit*	*Value (Cold Cavity)*	*Value (Hot Cavity)*
Mode Cleaner Length	m	16.681	
MC1 radius of curvature	m	>10000	-733
MC2 radius of curvature	m	26.900	27.92
MC3 radius of curvature	m	>10000	-733
MC1 Intensity Reflectivity		0.9985	
MC2 Intensity Reflectivity		0.99999	
MC3 Intensity Reflectivity		0.9985	
g-factor MC1		1.0	1.023
g-factor MC2		0.3799	0.4025
g-factor MC3		1.0	1.023
Cavity *g* factor		.3799	0.4212
Mirror absorption/scatter loss	ppm	50	
MC free spectral range	Hz	8986045[19]	
MC finesse		2073.7[20]	

[16] LIGO T000076-00-D, "Optical Layout for Advanced LIGO", D. Coyne

[17] LIGO T000087-01-D, "Available Height above the HAM Optics Table", D. Coyne

[18] Assumes replacement of HAM1,2 and HAM7,8 connecting beam tube with LIGO arm beam tube

[19] Uses c = 299792458 m/s in vacuum

MC waist	mm	2.102	2.114
Cavity Pole Frequency	Hz	4544	
Rayleigh range	m	13.06	13.99
Input Power	W	165	
Stored MC Power	kW	100	
MC mirror mass	kg	3.89	
MC mirror diameter	cm	15	
MC mirror thickness	cm	10	
Static Radiation pressure	N/m^2	0.000354856	

5.2.2 Physical Layout

The mode cleaner is a triangular cavity consisting of three suspended mirrors. There are two major changes from the LIGO I mode cleaner: slightly increased length and larger mass mirrors. The mode cleaner mirrors occupy HAMs 1 and 3 and have a 16-fold increase in mass.

5.3 Mode Cleaner Performance

5.3.1 Frequency Noise

Length fluctuations of the mode cleaner will compromise the frequency stability of the field leaving the mode cleaner. Figure 6 shows the expected total frequency noise performance and individual contributions to the MC frequency noise assuming the characteristics above.[21] The frequency stability is limited by technical radiation pressure noise over the entire frequency range. This stability and the allowed frequency noise of the field going into the main interferometer set the requirements on the frequency stabilization loop gains.

[20] including scatter loss

[21] LIGO T010002-00-D, "Reference Design Document for the Advanced LIGO Input Optics", G. Mueller, et al.

Figure 6 Expected Mode Cleaner Frequency Noise

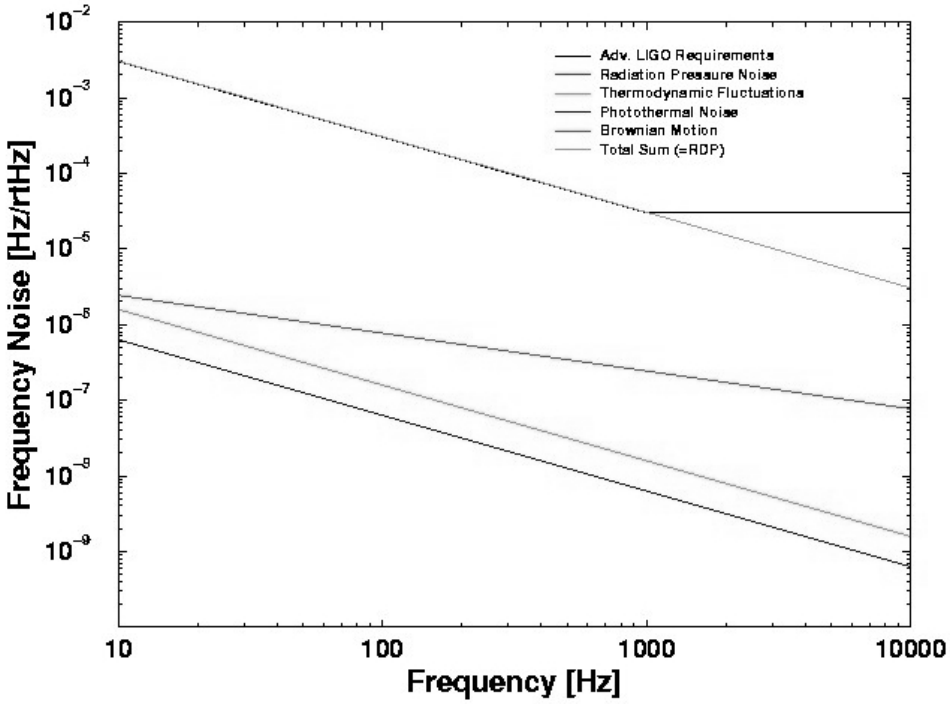

5.3.2 Beam Jitter Stabilization

The mode cleaner acts as a spatial filter and provides passive stabilization of time-dependent higher order spatial modes.[22] Assuming an input PSL jitter specification of 2 x 10^{-6} /$Hz^{1/2}$, Table 6 shows the attenuation of higher order modes (amplitude) through the MC for a cold and hot cavity.

Table 6 MC Beam Jitter Suppression

Mode index (n+m)	*Amplitude transmission*		*Suppression Factor*		*Output Amplitude Jitter*	
	Cold	**Hot**	**Cold**	**Hot**	**Cold**	**Hot**
1	0.00096	0.00100	1040	1004	1.92E-09	1.99E-09
2	0.00078	0.00077	1281	1304	1.56E-09	1.53E-09
3	0.00185	0.00146	540	687	3.70E-09	2.91E-09
4	0.00162	0.00243	616	412	3.25E-09	4.86E-09
5	0.00077	0.00082	1299	1222	1.54E-09	1.64E-09

[22] A. Rudiger, et al., Optica Acta **28**, 641 (1981).

6	0.00101	0.00085	986	1174	2.03E-09	1.70E-09
7	0.01190	0.00332	84	302	2.38E-08	6.63E-09
8	0.00092	0.00128	1089	782	1.84E-09	2.56E-09
9	0.00079	0.00076	1259	1317	1.59E-09	1.52E-09
10	0.00216	0.00108	462	927	4.33E-09	2.16E-09
11	0.00145	0.00875	689	114	2.90E-09	1.75E-08
12	0.00076	0.00093	1311	1075	1.53E-09	1.86E-09
13	0.00108	0.00078	928	1281	2.16E-09	1.56E-09
14	0.00596	0.00170	168	587	1.19E-08	3.41E-09
15	0.00088	0.00193	1135	519	1.76E-09	3.86E-09

5.3.3 Thermal Distortion in the Mode Cleaner

Absorption in coatings and the substrates of the mode cleaner mirrors will lead to changes in the effective radii of curvatures and change and distort the spatial eigenmode of the mode cleaner. The heating in the coating will change the sagitta δs across the beam profile of the mode cleaner mirrors. This change can be approximated as follows:

$$\delta s = \frac{\alpha}{4\pi\kappa} P_a$$

where α is the thermal expansion coefficient, κ is the heat conductivity and P_a is the absorbed power. Based on an absorption coefficient of 1ppm for the coatings, the fused silica mirror will change their sagitta by:

$$\delta s \approx 3nm$$

This would change the radii of curvatures of the flat mirror to -733 m, while the radius of curvature of the curved mirror would change from 26.9 m to 27.9 m (see Table 5).[23]

The substrate will act as a thermal lens for the input and output beams. This can be approximated by

$$\delta s = \frac{\partial n}{\partial T} \frac{P_a}{4\pi\kappa}$$

The absorption coefficient for fused silica is about 1ppm/cm. The subsequent effective sagitta change of the transmitted beam is:

$$\delta s \approx 1nm$$

[23] As these changes are anticipated, it is possible to polish the radii of curvatures of each MC mirror such that the loaded cavity has the correct eigenmode, as we have done for this design. The changes neither degrade the beam quality nor do the changes in the spatial eigenmode effect the mode matching significantly.

The induced focal length of about 1 km neither changes the beam quality nor affects the mode matching.

5.3.4 Alignment Procedure

The mode-cleaner alignment will use fixtures for installation of the suspended mirrors, fixed targets for initial beam alignment using the 1.064 μm PSL laser, in-air and in-vacuum resonance measurements for fine beam alignment, and measurements of the free spectral range for final length adjustment. (Details **TBD** pending detailed designs of the MC suspensions)

6 Faraday Isolator

6.1 Introduction

The Faraday Isolator rejects back-reflected light from the COC and directs the light to ISC photodetectors for length and alignment sensing.

6.2 High Power Design

The power increase in Advanced LIGO will cause increased thermal lensing and thermally-induced birefringence in the Faraday isolator. Excessive thermal lensing could potentially introduce uncompensatible higher order modes; the magnitude of these modes determines the placement of the FI (before or after the MC). Excessive thermal birefringence leads to decreased optical isolation.

The optical isolator design shown in Figure 7 has been tested as a prototype for Advanced LIGO. In this design, two 22.5° Faraday rotators and a reciprocal quartz polarization rotator placed between them replace the traditional single crystal 45° Faraday rotator.[24] In such a configuration, polarization distortions that a beam experiences while passing the first rotator, will be compensated in the second.

Figure 7 Faraday Isolator Design

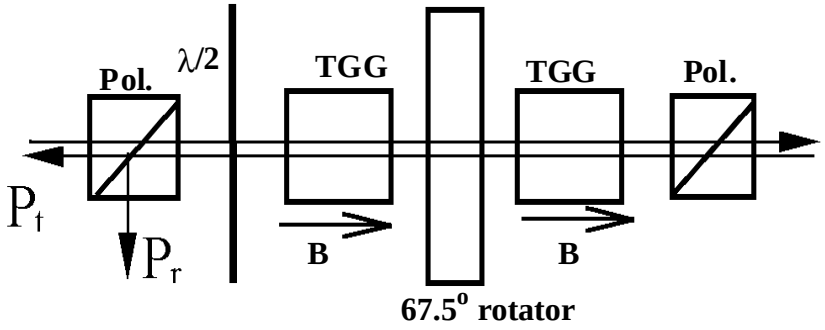

6.3 Isolation Performance

This device has been tested at powers up to 85 W (double pass). The results (shown in Figure 8) are quite promising. We were able to achieve an isolation ratio of 45 dB over the 0-85 W range.

[24] E. Khazanov, N. Andreev, A. Babin, A. Kiselev, O. Palashov, and D. H. Reitze, "Suppression of Self-Induced Depolarization of High-Power Laser Radiation in Glass-Based Faraday Isolators, J. Opt. Soc. Am B. **17**, 99-102 (2000).

Figure 8. Comparison of FI Designs

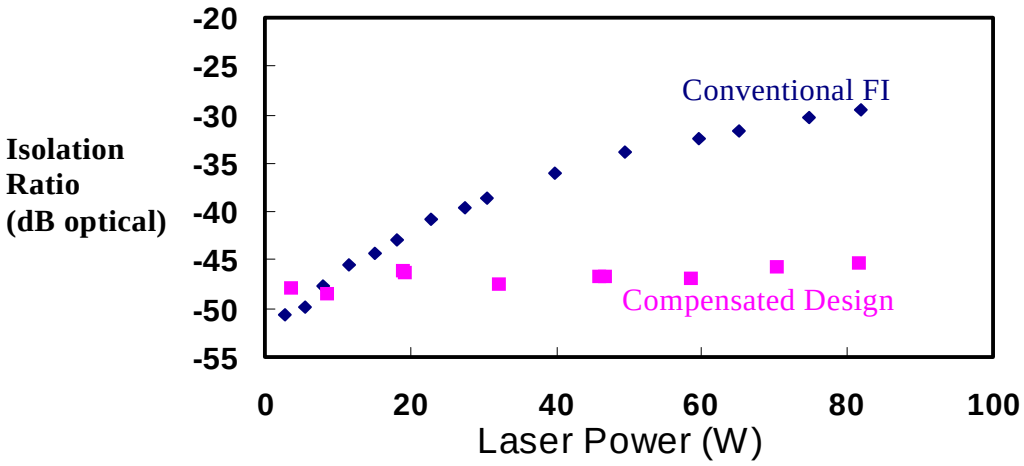

6.4 Stray magnetic fields

Estimations of magnetic strength from LIGO isolators have been made.[25] Permissible leakage magnetic field from the Faraday Isolator is TBD pending actuation.

6.5 Vacuum compatibility

Vacuum compatibility tests of Faraday magnets and other components will be carried out using the on-site vacuum bake ovens at LLO or LHO. Components suitable for testing will be acquired from vendors and evaluated during the final design period.

6.6 Passive compensation of thermal lensing

As in LIGO I, the Faraday isolator will be located after the mode cleaner to decouple the mode cleaner from the interferometer. The Faraday isolator could in principle be located in front of the mode cleaner. However, during IFO lock acquisition the power in the reflected field coming from the interferometer will change from 120W to 0W on relatively fast time scales. This reflected field will be resonant in the mode cleaner and change the radiation pressure. To compensate these changes, the mode cleaner longitudinal feedback loop would require a large bandwidth and slew rate. **We believe that this outweighs the advantages of lower spatial mode distortion and better accessibility of having the isolator in front of the mode cleaner.** With 125 W of CW power transmitting through the TGG crystal, modal distortions will occur as the laser beams heats the crystal. But our tests indicate so far that the thermal compensation scheme described below will reduce these distortions below the required level.

6.6.1 Measurement of Thermal Lensing

The beam distortion and the thermal lens in a TGG-based Faraday Isolator were measured using a 50W Nd:YLF pump laser and a 500mW NPRO probe laser. The changes in the spatial mode of the

[25] YOSHIDA DOCUMENT

probe laser were analyzed with an analyzer cavity and measured with respect to the power in the pump beam.[26] The results were in good agreement with theoretical models and showed that the beam distortion would reduce the TEM_{00} mode content in Advanced LIGO to approximately 66% assuming typical TGG absorption coefficients. A bullseye mode makes up most of the higher order modal content (approximately 25%) and thus can be recovered by adjustment of the mode matching telescope. The remaining higher order modes (approximately 10% of the total power) cannot be recovered by the MMT. To minimize these effects, a passive compensation technique has been developed.

Figure 9 Mode Content versus Power in TGG Using a Thermal Lens Compensator

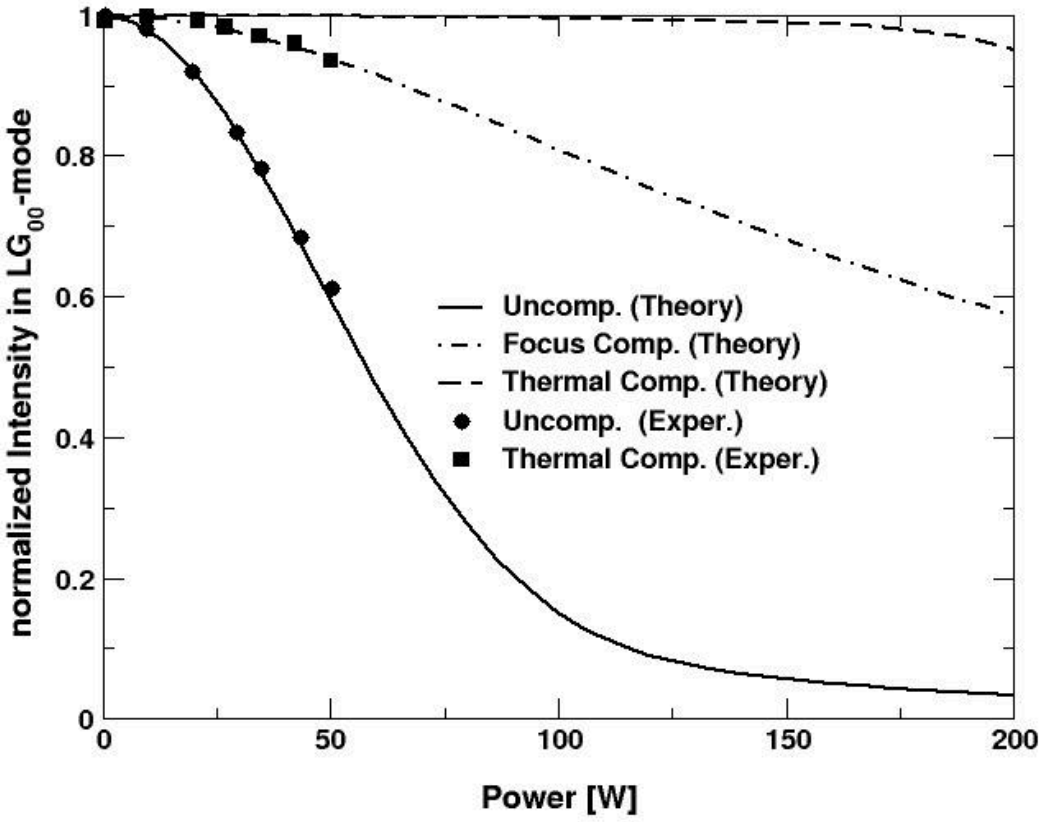

[26] "Method for Compensation of Thermally-induced Modal Distortions in the Input Optical Components of Gravitational Wave Interferometers," G. Mueller et al., accepted for publication in a special issue of *Classical and Quantum Gravity*, to appear, 05/2002.

Figure 10 Mode Content versus Power with Compensation and Focal Adjustment

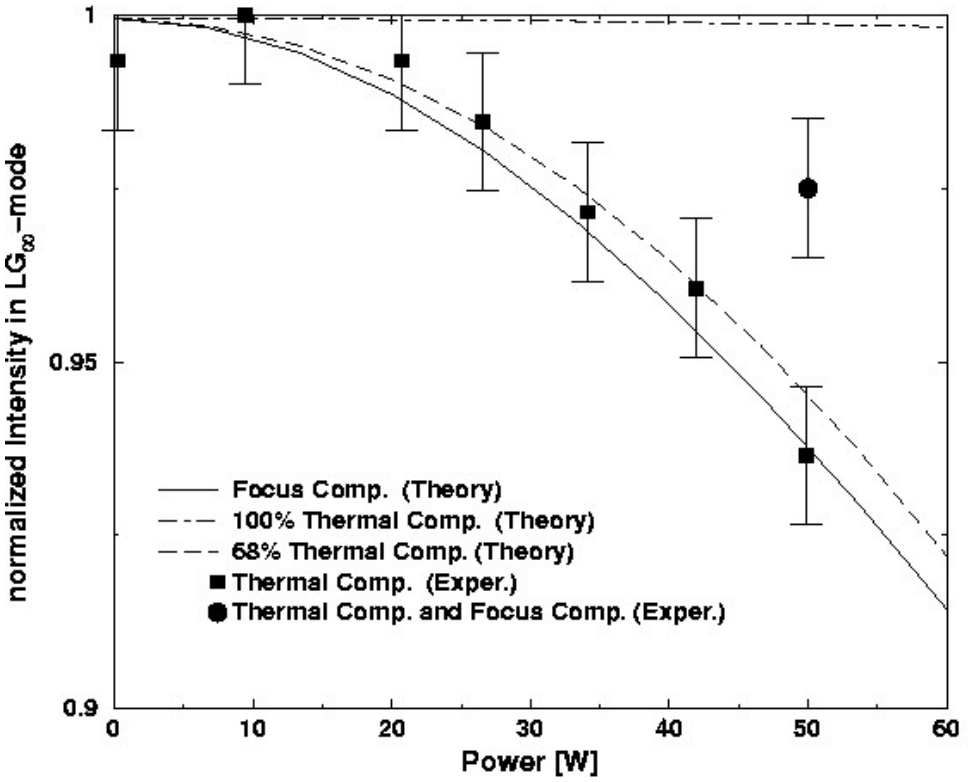

6.6.2 Passive Compensation of Thermal Lensing

The thermal deformation in optical crystals can be compensated with a second crystal that imprints the opposite spatial phase distortion on the beam.[27] This can be done passive with a glass with a negative *dn/dT* like the Schott glass FK51. The compensator optical path length must be matched to the actual crystal parameters (absorption coefficient). Since the optical absorption can vary from sample to sample in TGG, our initial tests were performed using a variable length compensator consisting of two anti-parallel prisms.

The results are shown in Figure 9 and Figure 10. Figure 9 shows the output power dependent modal content. The solid line is a theoretical prediction based on the known thermal conductivity and absorption coefficient in TGG. The circles are the data versus power. In our experiments, the absorption coefficient in the TGG in the isolator was unusually large (a factor of 3 times literature values). Thus, while we report the actual power on the x-axis, the level of absorption is such that the maximum power would correspond to 150 W in a typical TGG crystal. For an uncompensated isolator, roughly 40% of the power is lost into higher order modes at this high absorbed power. The dashed line shows the prediction of the compensation in an ideal case where the optical paths of the TGG and compensator are matched. The dash-dot line corresponds to the removing the

[27] "Method for Compensation of Thermally-induced Modal Distortions in the Input Optical Components of Gravitational Wave Interferometers," G. Mueller et al., accepted for publication in a special issue of *Classical and Quantum Gravity*, to appear, 05/2002.

residual bullseye mode by adjusting the downstream mode-matching into the analyzer cavity. The squares show the compensated data using the maximum length of FK51 available in our experiments. While the data corresponds to the theoretical curve for bullseye removal, it is important to emphasize this data represents a pure passive compensation; no adjustments were made to optimize the mode-matching.

To emphasize this, Figure 10 displays the thermal compensation data (squares) compared to partial passive compensation (dashed line). Since only partial compensation was achieved (limited by the FK51 physical dimensions), it was possible to further optimize the mode by adjusting the mode matching. The round data point depicts the experimental result, showing 97.5% of the light in the TEM_{00} mode. Thus, while complete compensation of the thermal lensing could not be achieved due to limited optical path in the FK51, compensation from 66% mode matching to 97.5% mode matching could be demonstrated. With larger FK51 paths, we believe that better results can be achieved.

6.7 Placement of FI on HAM Stack

Since the Faraday isolator will be located between the MC and PRM, the vibrational motion of the FI will add frequency noise to the laser through the Fizeau effect. We have examined the frequency noise imparted to the laser if the Faraday is mounted directly to the HAM table without suspension.

The total phase accumulation during propagation through the FI is given by:

$$\phi = \frac{2\pi\nu}{c} nL = 2\pi\nu \frac{L}{V}$$

where ν is the light frequency, n is the index of refraction in the medium, c is the speed of light in vacuum, and $V=c/n$ is the speed of light in the medium. The motion of the isolator in the lab imparts a phase shift through the Fizeau effect:

$$\delta\phi = -2\pi\nu\, L \frac{\delta V}{V^2}$$

$$V = \frac{c}{n} + V_{FI}\left(1 - \frac{1}{n^2}\right) \approx \frac{c}{n}; \qquad \delta V = \delta V_{FI}\left(1 - \frac{1}{n^2}\right)$$

where $V_{FI}, \delta V_{FI}$ are the velocity and velocity fluctuations of the FI due to motions of the HAM table. Combining these, and using $\delta V_{FI} = 2\pi f\, \delta x_{siesmic}$, we find

$$\delta\phi = -(2\pi)^2\, f\nu\, L \frac{\left(n^2 - 1\right)}{c^2} \delta\, x_{seismic}$$

where f is the (low) frequency of the HAM motion and $\delta x_{siesmic}$ is the displacement fluctuation. Using $\delta f = 2\pi f\, \delta\phi$ and taking the amplitude spectral density of the seismic motion ($\delta x_{siesmic}$ = 2 x 10^{-13} m/rHz at 10 Hz and falling roughly as $1/f^2$)[28], we find

$$\delta\, f = 1.5x10^{-12} \frac{Hz}{\sqrt{Hz}} \left(\frac{10Hz}{f}\right)^2 \left(\frac{\delta\, x_{seismic}}{2x10^{-13}}\right)$$

[28] LIGO-E010016 "Advanced LIGO Seismic Isolation System Conceptual Design," R. Adhikari, et al.

This is well below the frequency noise of the mode cleaner. Therefore, we can place the FI directly on the HAM table.

7 Mode Matching

Mode matching in the input optics consists of:

- mode matching into the mode cleaner
- mode matching from the mode cleaner to the IFO

The mode matching must be adjustable to accommodate any deviations in core and telescope optics specifications. In addition, it must provide for mode matching for both operational powers of the IFO. In addition, it must not add additional pointing drift or jitter to the laser beam.

7.1 Mode Cleaner Mode Matching

The baseline system resembles closely the LIGO I design based on a three lens configuration. (**TBD PENDING DETAILED LAYOUT OF THE PSL AND MC.**)

7.2 COC Mode Matching

The Input Optics provides a beam to the IFO with mode characteristics determined by the fundamental (Gaussian) mode parameters of the Fabry-Perot arm cavities. The telescope must provide a beam that is 95% TEM_{00} in the FP cavities.

Unlike LIGO I, the baseline design for the Advanced LIGO MMT consists of only two mirrors. The nominal spatial eigenmode of the arm cavities is defined by the required 6 cm beam size on each test mass. There are two possible solutions to achieve this. The baseline design requires 55 km radii of curvatures of the test masses, while the other solution would require 2.1 km radii of curvatures. A nominal solution for the mode matching for the baseline design can be found in the following table. The first three values are the distances between mode cleaner waist (MC) and first telescope mirror (MMT1), between the two telescope mirrors (MMT1, MMT2), and between the last telescope mirror and the power recycling mirror (PR). The last two values are the radii of curvature of the telescope mirrors. This nominal solution needs to be modified pending results of thermal deformation measurements of core optical components and MELODY simulations of the full interferometer and constrains imposed by available real estate. (TBR)

MC -> MMT1	MMT1-> MMT2	MMT2 -> PR	RC (MMT1)	RC (MMT2)
15.4 m	13.0 m	18.0 m	-1.55 m	27.505 m

The mode matching efficiency changes quadratic with the distance between the two mode matching mirrors. The non mode-matched power is:

$$P_{HM} \approx \left[\frac{d}{[cm]}\right]^2 \times 0.073 \times P_{IN}$$

7.2.1 Adaptive In Situ Telescope Adjustment

It is possible to adjust the IFO mode matching *in situ* by purposely creating a thermal lensing in large bandgap semiconductor doped glass using by a short wavelength laser to modify the mode-matching of the main laser beam. The basic concept is illustrated in Figure 11. A thin (1-3 mm)

plane parallel glass which is highly absorbing at short wavelengths and transmissive at long wavelengths serves as the first 'lens' in the MMT. The adjustable lens is created by the absorption of 532 nm light (other wavelengths could be easily used) from a laser located outside the vacuum chamber. Polarization multiplexing is used to switch the heating laser into and out of the main beam. To suppress higher order mode introduction into the AdL laser, the waist of the 532 nm light at the lens is roughly 4-5 times larger, such that the 1064 nm light samples the central, spherical portion of the thermal lens created by the absorbed laser.

Figure 11. In Situ Adjustment of Mode Matching

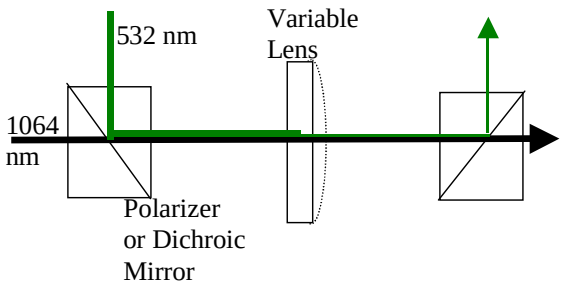

A (very) conceptual design is as follows:

- variable lens[29]
  - material: OG590 Schott glass
  - transmittance @ 532 nm: <0.00001 $P_{incident}$
  - transmittance @ 1064 nm: >0.9999 $P_{incident}$
  - thickness: 3 mm
  - thermal conductivity: 1.4 W/(m K)[30]
  - thermal expansion: 1.07 x 10^{-5}/K
  - dichroic AR coatings for 1064 and 532 nm
  - mounted directly on HAM table[31]
  - scatter: Bubble class 1 (0.03 – 0.10 mm^2 of cross sectional area for 100 mm^3 volume)
- heating laser
  - intracavity frequency doubled Nd:VO_4 operating at 532 nm
  - maximum power: 10 W
  - amplitude and pointing stability requirements: TBD

[29] Data taken from Schott Optical Glass Filter catalog

[30] thermal conductivity for OG590 not listed; assumes fused silica

[31] see analysis on p. 35, "Placement of FI on HAM Stack"

  - waist size at variable lens: ~ 6 mm
- optical path changes[32]
  - waist of 1046 nm at variable lens: 3 mm
  - ΔOPD @ 532 nm: ~10^{-6} m/W
  - ΔOPD @ 1064 nm: ~0.3 x 10^{-6} m/W
  - effective focal length range for 1064 nm: + 9.4 m to infinity

In order to assess the feasibility of this method, we will undertake a detailed design study during the Preliminary Design phase. The following steps are planned:

- Detailed MMT design based on variable lens and two mirrors
- Thermal modeling
  - determination of optimum 532/1046 waist ratio
  - determination of high order modal contamination at full 532 laser power
  - MMT performance (mode matching range)
- Prototype tabletop mode-matching experiment using variable lens and fixed lens
  - 25 W argon laser pump
  - 1064 NPRO probe
  - measure of light scatter @ 532 and 1064 nm
  - FP analyzer cavity to measure:
    - mode-matching range
    - higher order mode content
    - thermal time constants

7.3 Alignment Procedure

The initial procedure will be the same as for the mode cleaner: installation fixtures followed by the use of targets attached to the suspensions. Final alignment will be carried out by measuring the errors in mode-matching to the IFO.

[32] Assumes 3 mm thick optic; can be made larger by increasing glass path.